OPEN ACCESS
IOP Publishing
Journal of Physics: Condensed Matter
J. Phys.: Condens. Matter **32** (2020) 165801 (11pp)
https://doi.org/10.1088/1361-648X/ab678c

Impact of growth kinetics on the interface morphology and magnetization in $La_{1/3}Sr_{2/3}FeO_3/La_{2/3}Sr_{1/3}MnO_3$ heterostructures

M Waschk[1], A Sarkar[1], J Barthel[2], J Voigt[1], S Schröder[1], P Zakalek[1], M Schmitz[1], B J Kirby[3], S Pütter[4], J Schubert[5] and T Brückel[1]

[1] Forschungszentrum Jülich GmbH, Jülich Centre for Neutron Science (JCNS-2) and Peter Grünberg Institut (PGI-4), JARA-FIT, 52425 Jülich, Germany
[2] Forschugszentrum Jülich GmbH, Ernst Ruska-Centre for Microscopy and Spectroscopy with Electrons (ER-C-2), 52425 Jülich, Germany
[3] NIST Center for Neutron Research, National Institute of Standards and Technology, Gaithersburg, MD 20899, United States of America
[4] Forschungszentrum Jülich GmbH, Jülich Centre for Neutron Science JCNS at Heinz Maier-Leibnitz Zentrum MLZ, 85748 Garching, Germany
[5] Forschugszentrum Jülich GmbH, Peter Grünberg Institut (PGI-9) and JARA-Fundamentals of Future Information Technology, 52425 Jülich, Germany

E-mail: a.sarkar@fz-juelich.de

Received 17 October 2019, revised 2 December 2019
Accepted for publication 3 January 2020
Published 17 January 2020

Abstract

The ability to create atomically perfect, epitaxial heterostructures of correlated complex perovskite oxides using state-of-art thin film deposition techniques has generated new physical phenomena at engineered interfaces. Here we report on the impact of growth kinetics on the magnetic structure and exchange coupling at the interface in heterostructures combining layers of antiferromagnetic $La_{1/3}Sr_{2/3}FeO_3$ (LSFO) and ferromagnetic $La_{2/3}Sr_{1/3}MnO_3$ (LSMO) on (0 0 1)-oriented $SrTiO_3$ (STO) substrates. Two growth orders are investigated, (a) LSMO/LSFO/STO(0 0 1) and (b) LSFO/LSMO/STO(0 0 1), where the LSFO layer is grown by molecular beam epitaxy and the LSMO layer by high oxygen pressure sputtering. The interface has been investigated using electron microscopy and polarized neutron reflectometry. Interdiffusion over seven monolayers is observed in LSMO/LSFO (a) with an almost 50% reduction in magnetization at the interface and showing no exchange coupling. However, the exchange bias effect ($\mu_0 H_E = -2.35$ mT at 10 K) could be realized when the interface is atomically sharp, as in LSFO/LSMO (b). Our study therefore reveals that, even for well ordered and lattice-matched structures, the kinetics involved in the growth processes drastically influences the interface quality with a strong correlation to the magnetic properties.

Keywords: magnetic depth profile, exchange bias, polarized neutron reflectivity, growth kinetics, interface diffusion, thin film heterostructure, epitaxy

(Some figures may appear in colour only in the online journal)

1. Introduction

Transition metal oxides (TMO) with the perovskite structure (ABO_3) exhibit a wealth of interesting phenomena due to their complex electronic structure, and are highly sensitive to external influences like strain, electric, or magnetic fields [1]. Interfaces in heterostructures of this material class, due to reconstructions of charge, orbital and spin states on atomic scale often give raise to exotic properties, which cannot be found in their bulk counterpart or single layers [2]. Especially TMO heterostructures with ferromagnetic/antiferromagnetic (FM/AF) interfaces are of great interest due to exchange coupling, which is not only significant from a fundamental perspective, but also for industrial applications. However, because of the strong coupling among different degrees of freedom, physical properties can be largely altered at the interface, which can be crucial for functionalities but challenging to predict. For example, suppressed magnetization at the interface can produce inferior device performance [3]. There are lasting efforts to understand its origin and eliminate this effect [4, 5]. Furthermore, novel magnetic coupling and emergent interfacial magnetization can strongly affect functionalities, including exchange bias [6, 7] and spin-dependent transport [8, 9]. Therefore profound understanding of various oxide interface physics will certainly contribute to utilize these intriguing properties for applications.

Heterostructures of lanthanum strontium manganite ($La_{1-m}Sr_mMnO_3$) and ferrite ($La_{1-n}Sr_nFeO_3$) are interesting systems to study electronic doping effects on magnetic interfaces and their influence on transport properties, FM/AF coupling effects, and influence of the interface morphology on the physical properties like magnetism. $La_{1-m}Sr_mMnO_3$, on one hand, is well-known for its rich magnetic, electronic, and structural phase diagram [10–13]. Its high sensitivity to strain [14, 15], doping [16–18], magnetic fields, and growth thermodynamic [19] makes it an ideal candidate to investigate proximity effects at interfaces. Especially, $La_{2/3}Sr_{1/3}MnO_3$ (LSMO) is a half-metallic ferromagnetic conductor with a Curie temperature of $T_C = 360$ K [20]. A strong correlation between the structural and magnetic properties of LSMO has also been reported to exist [16–18]. $La_{1-n}Sr_nFeO_3$, on the other hand, is another interesting perovskite oxide with different physical phase transitions. It crystallizes in the space group $R\bar{3}c$ with a deviation of 0.01° from ideal cubic structure and therefore can be expressed in a pseudo-cubic representation. The charge and magnetic propagation vector points to the [1 1 1] direction of the pseudo-cubic unit cell [21]. Stoichiometric $La_{1/3}Sr_{2/3}FeO_3$ (LSFO) is an antiferromagnetic insulator [21, 22] and shows a significant resistivity change at 195 K similar to the known Verwey transition in magnetite [23]. The transition is accompanied by a charge disproportionation ($2Fe^{4+} \rightarrow Fe^{3+} + Fe^{5+}$), paramagnetic to antiferromagnetic phase transition, and charge ordering [24, 25]. It is observed that the Verwey transition in LSFO thin films is strongly correlated to its stoichiometry [26] and a critical thickness (∼40 nm) exists below which the transition is smeared out and vanishes for very thin layers [27].

In thin films of both LSMO and LSFO, the magnetic properties are observed to be highly sensitive to the change in the electronic structure [10] or applied strain [14]. The influence of epitaxial strain can already be minimized at the film/substrate interface by growing films epitaxially on lattice matched $SrTiO_3$ (STO) substrates. Moreover, both LSMO and LSFO, exhibit the pseudocubic perovskite structure with a difference in bulk lattice constants of ∼0.1% [28]. This enables the observation of an LSMO/LSFO interface with a minimum of applied strain. However, the different magnetic phases (FM and AF) are coupled to a different balance of superexchange and double exchange for the different average valencies of Fe (+3.33) and Mn (+3.67). Due to such coupling, moving the system through the Verwey transition of LSFO, one expects to change charge ordering viz. the electronic states at the interface and therefore would be interesting to investigate the response of the ferromagnetic LSMO.

In this work we report on the growth and characterization of heterostructures of antiferromagnetic $La_{1/3}Sr_{2/3}FeO_3$ (LSFO) and ferromagnetic $La_{2/3}Sr_{1/3}MnO_3$ (LSMO), with a focus to understand (a) the impact of growth kinetics on the interface morphology and magnetization, and (b) the influence of the different charge ordered states of the LSFO on the magnetic properties of the LSMO. The particular stoichiometries have been chosen so that LSMO is a ferromagnetic conductor ($T_C = 360$ K), while LSFO exhibits the Verwey transition ($T_V = 195$ K) and is antiferromagnetic below this, with Néel temperature corresponding to $T_N = T_V$ [29]. Using standard microscopic and macroscopic methods the structure and magnetic properties of the heterostructures have been characterized. Further, the interface has been extensively probed by means of electron microscopy and polarized neutron reflectivity, from which we derive a correlation between the morphology and magnetic properties of the interface.

2. Experimental

The heterostructures were grown on (0 0 1)-oriented $SrTiO_3$ (STO) single crystal substrates, by a combination of oxide assisted molecular beam epitaxy (MBE), and high oxygen pressure sputtering (HOPS). For the present study, two different heterostructures have been prepared—(i) LSFO/LSMO/STO(0 0 1) referred to as LSFO-final and (ii) LSMO/LSFO/STO(0 0 1) referred to as LSMO-final, henceforth in this article. The LSFO-final was fabricated by growing LSFO using oxide MBE onto a sputtered LSMO film, while the LSMO-final was fabricated by sputtering LSMO film onto an oxide MBE grown LSFO layer, respectively on STO(0 0 1).

The single crystalline bulk STO(0 0 1) substrate due to its high elasticity (∼217 GPa along ⟨1 0 0⟩), compared to that produces by the initial few monolayers of the film (LSMO or LSFO), allows a well controllable growth along the in-plane [1 0 0]/[0 1 0] direction. Homogeneous growth of the layers was optimized by characterizing the layer properties individually using various macroscopic and microscopic methods, and compares well to the available literature [14, 27]. The thicknesses were initially calibrated and optimized for each layer

independently for a fixed growth rate and deposition time. This was then used to grow the final heterostructures and less than 5% (max. ± 1 nm) deviation from the optimized thickness was observed. Therefore, for both the heterostructures well controllable and epitaxial growth were achieved along all the three $\langle 1\,0\,0 \rangle$ directions.

LSFO was grown (using MBE) under an oxygen partial pressure of 1×10^{-7} mbar (mass flow $\sim$0.15 standard cubic centimeters per minute) where individual elements (e.g. La, Sr, and Fe) were evaporated from respective effusion cells at controlled rates. To obtain the desired stoichiometry and thickness, rates were calibrated using a quartz crystal microbalance and were verified using Rutherford backscattering spectrometry (RBS).

The slow growth rate of 0.05 Å s^{-1} ensures a good surface morphology and oxygen saturation. Before deposition the STO(0 0 1) substrate was annealed at 1320 K for 1 h and subsequently the film was grown at a temperature (T_g) of 1240 K. A post-annealing step at growth temperature for 1 h was introduced which significantly increased the surface quality with respect to (w.r.t.) the roughness and crystallinity. The sample was then cooled slowly (3 K min^{-1}) to room temperature in oxygen which ensures proper saturation of oxygen within the LSFO layer. For LSFO grown as the second layer on LSMO/STO(0 0 1) the post-annealing time was reduced to 15 min in order to avoid interdiffusion between substrate and layer as well as desorption of atoms which influences the surface stoichiometry.

For the sputtering of LSMO a commercially available stoichiometric target (Kurt J. Lesker Ltd.) was used. The sputtering process was initiated at 2 mbar oxygen pressure with a radio-frequency (rf) plasma power of 120 W which results in a growth rate of 0.04 Å s^{-1} for a substrate to target distance of 3 cm. This rate is comparable with the growth rate used for preparation of LSFO. A T_g of 1250 K has been used after annealing the substrate at 1250 K for 1 h. Similar to the case mentioned above, for the sample where LSFO is already deposited on the substrate the pre-annealing time was shortened to 15 min. A post-annealing was also added with the same parameters as used for the deposition of LSFO. A detailed description of sample growth can be found elsewhere [29].

In situ reflection high-energy electron diffraction (RHEED) as well as low-energy electron diffraction (LEED) reveal smooth and crystalline surfaces of the thin film layers (not shown here). The surface quality has also been checked after in-air transport of the sputtered LSMO film to MBE chamber under ambient conditions. The clean LEED pattern with sharp spots and low background of the sputtered LSMO film is shown in figure 1, indicating a smooth and clean surface. We may conclude that the high stability of transition metal oxides makes it possible to combine two growth techniques to achieve high quality heterostructures with well defined stoichiometry.

The crystalline quality and surface morphology was further analyzed using *ex situ* x-ray diffractometry (XRD) and reflectometry (XRR) measured with a Bruker D8 Advance with a Cu–K_α wavelength of $\lambda = 1.54$ Å. The magnetization

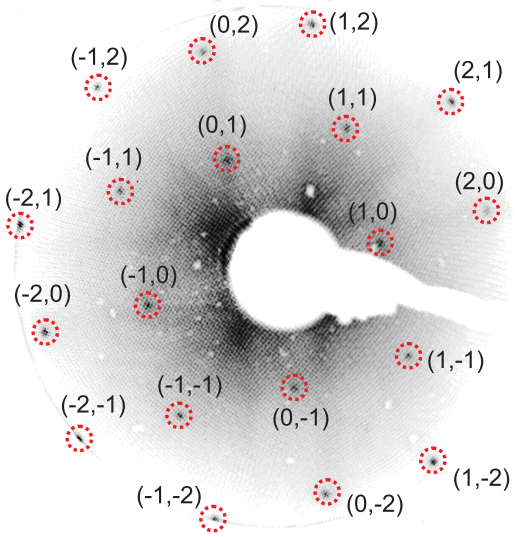

Figure 1. Low energy electron diffraction pattern taken at 100 eV of a LSMO sample after in-air transfer from the sputtering system to the MBE system. The observable planes are marked with red circles for better viewing.

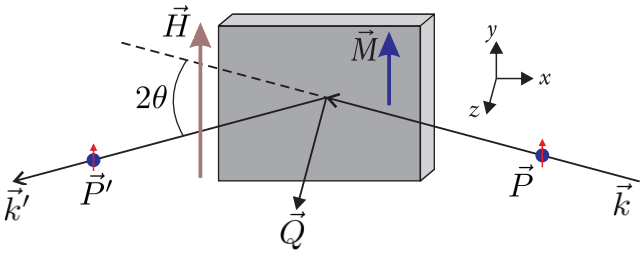

Figure 2. Scattering geometry of a polarized neutron reflectometry experiment. Incident beam with wave vector $\vec{k}$ and polarization $\vec{P}$ is reflected from a sample. The magnetization of the sample (magnetic saturation reached by an applied magnetic field $\vec{H}$) is parallel to the polarization of the incoming neutrons. In saturation, the polarization $\vec{P}'$ of the reflected beam $\vec{k}'$ is identical to the incident polarization $\vec{P}$. 2θ equals the angle between incident and the reflected beam. The wavevector transfer $\vec{Q}$ ($= \vec{k}' - \vec{k}$) is directed perpendicular to the sample plane and therefore $\perp \vec{M}$.

measurements were carried out using a superconducting quantum interference device (SQUID) magnetometer (Quantum Design). The magnetization of individual layer in the heterostructure was independently characterized on STO(0 0 1). LSFO being antiferromagnetic revealed very week response, while LSMO being highly ferromagnetic showed good magnetic response to the external magnetic field. For the thickness ($\sim$20 nm) of LSMO, as used in the heterostructures, saturation magnetization was obtained to be 3.4 μ_B/Mn atom compared to 3.7 μ_B/Mn atom for the bulk, where μ_B is the Bohr magneton. However, the difference in magnetic properties (compared to bulk material) and its dependence on the film thickness being obvious and very well studied by many researchers [30], in this article we emphasize mainly on multilayer and magnetic interactions between them.

In order to probe the depth resolved magnetization profile, polarized neutron reflectometery (PNR) measurements [31] were carried out on the polarized beam reflectometer (PBR) at the NIST Center for Neutron Research [32]. A sketch of

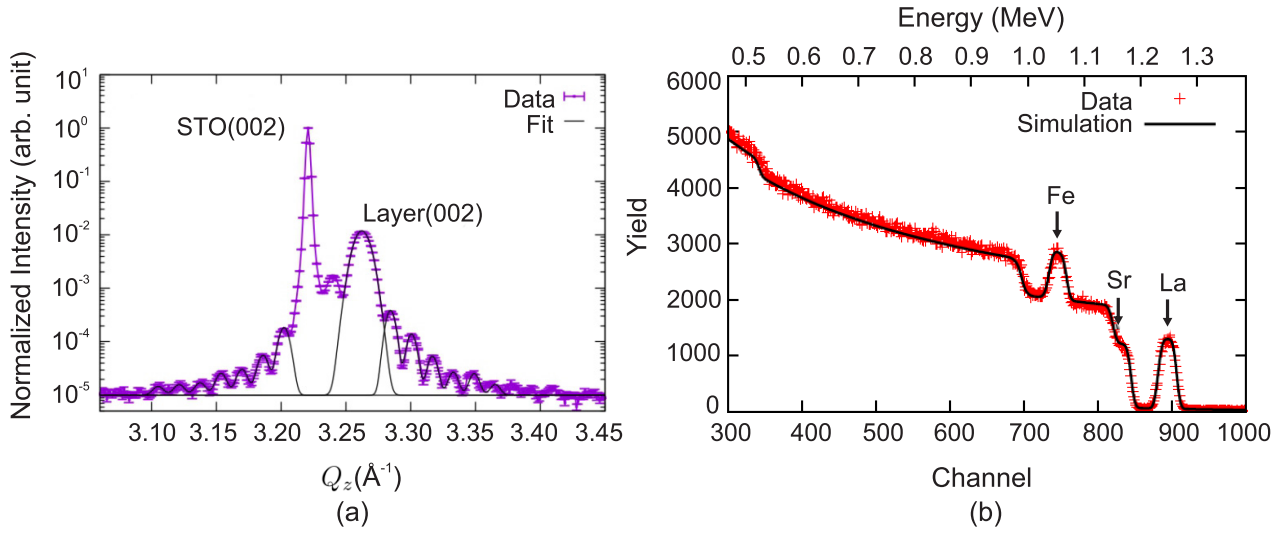

Figure 3. (a) XRD of LSFO-final heterostructure where the intensity has been normalized to the maximum intensity of the STO(002) peak, and (b) RBS measurement of a single LSFO layer, where the number of detected backscattered particles (Yield) is plotted as a function of the particle energy (in MeV).

the PNR measurement geometry is shown in figure 2, where the wavevector transfer Q (the difference between the incident, $\vec{k}$ and specularly reflected, $\vec{k}'$ neutron wavevectors) lies parallel to the direction of surface normal (z-axis). A neutron beam with polarization ($\vec{P}$) impinges on the sample surface and after reflection its polarization ($\vec{P}'$) is analyzed. The direction, i.e. up and down, of the neutron spin-polarization are generally represented by $+$ and $-$, respectively. The corresponding interference pattern as a function of Q (due to reflection from the sample surface) is obtained and represented by the spin-dependent reflectivities $R(Q)$ as, (a) two non spin-flip (R_{++} and R_{--}) reflectivities, where both ($\vec{P}$ and $\vec{P}'$) have same orientation, either $++$ or $--$, resulting due to the component of sample magnetization ($\vec{M}$) parallel to the neutron polarization ($\vec{M}||\vec{P}$), and (b) two spin flip (R_{+-} and R_{-+}) reflectivities, where both are opposite ($+-$ or $-+$) indicating a spin-flip processes/scattering at the sample due to magnetization component lying perpendicular to the neutron polarization ($\vec{M} \perp \vec{P}$). As magnetic neutron scattering probes only the component of magnetic moment perpendicular to the momentum transfer (Q_z), the method is sensitive to ordered moment parallel to the film surface (i.e. in the $x-y$ plane).

For our measurements, the sample was probed with spin-polarized neutron beam of wavelength 4.75 Å and an in-plane magnetic field ($\mu_0 H$) of 110 mT was applied to ensure saturation of the sample magnetization ($\vec{M}$) parallel to the polarization ($\vec{P}$) of the incoming neutrons (i.e. $\vec{M}||\vec{P}$ always), therefore measuring only the non-spin flip reflectivities (R_{++} and R_{--}). It must be noted that the two different non-spin flip reflectivities, R_{++} and R_{--}, result from the fact that for one spin-polarization (in this case $+$) the nuclear (N) and magnetic (M) scattering length density (SLD) adds up, while for the other ($-$) they are subtracted. Therefore, from the difference one can model the depth resolved structure as well as the laterally averaged in-plane magnetization of the heterostructure.

The structure and morphology of the interface has been studied using high-resolution scanning transmission electron microscopy (STEM) which was performed with an FEI Titan G2 80–200 [33], operated at 200 kV accelerating voltage. The scanning electron probe of 0.5 nA current was focused to full-width-at-half-maximum (FWHM) of about 1.2 at the surface of the cross-section sample using spherical aberration correction. STEM images were recorded from less than 50 nm thin cross-section samples with an annular detector placed in the high-angle annular dark-field regime (HAADF). A windowless energy dispersive x-ray (EDX) detection system was used to measure EDX maps [34] which were used to study the interdiffusion at the interface. The STEM-HAADF images were recorded within 20 s with the primary beam electrons, whereas 15–20 min mapping time was used for the high-resolution EDX in order to achieve atomic-scale resolution with the comparatively weak and element specific secondary x-ray emissions.

3. Results

3.1. Structural characterizations

The out-of-plane XRD measurement of STO (002) and layer (002) reflection for LSFO-final is shown in figure 3(a), where the intensity has been normalized to the STO(002) peak. Similar results were obtained for the LSMO-final. As both, the LSMO and the LSFO layers have similar crystal structure, the (002) LSMO reflection coincides with that of the LSFO. The average out-of-plane lattice constant c of the layers are obtained to be 3.855(1) Å for LSMO-final and 3.852(1) Å for LSFO-final, respectively, indicating a pseudo-cubic perovskite structure [35, 36].

Due to the low x-ray contrast between the scattering lengths of LSFO and LSMO, the bi-layer results in a diffraction pattern with a central (002) reflection and a large

Table 1. Film thickness (d) and roughness (σ) evaluated from XRR measurements and simulation, where all the values are in Å unit. For comparison total thickness (d_{tot}) obtained from XRR and XRD thickness oscillations is shown.

		LSMOfinal	LSFOfinal
LSFO layer	d	$214.7^{+0.7}_{-0.5}$	$207.3^{+0.5}_{-0.5}$
	σ	$4.3^{+0.5}_{-0.2}$	$5.2^{+0.2}_{-0.4}$
LSMO layer	d	$182.7^{+1.4}_{-0.3}$	$192.9^{+0.9}_{-0.6}$
	σ	$5.3^{+0.5}_{-0.1}$	$4.0^{-0.1}_{+1.0}$
Surface layer	d	$21.4^{+0.2}_{-0.2}$	$16.7^{+0.2}_{-0.4}$
	σ	$8.4^{+0.1}_{-0.2}$	$5.2^{+0.1}_{-0.1}$
Total thickness (d_{tot})	XRR	419^{+2}_{-2}	417^{+2}_{-2}
	XRD	407^{+2}_{-2}	388^{+2}_{-2}

number of thickness oscillations. The oscillations are indicative of a high degree of crystallinity in the growth direction and sharp interfaces to the substrate and vacuum. The oscillation period corresponds to the thickness of the crystalline part of the layer (see table 1) and is an evidence that the whole stack exhibits out-of-plane crystallinity. The stoichiometry of the LSFO and LSMO films were further confirmed from the RBS measurements. Figure 3(b) shows a typical RBS measurement for a single LSFO layer revealing a stoichiometry of $La_{0.33}Sr_{0.66}FeO_{3-\delta}$, obtained from the simulation of the data. As the RBS technique can not precisely determine the oxygen content, for both the LSMO and LSFO thin films the exact oxygen stoichiometry could not be determined. However, from the magnetic and transport properties of the films a stoichiometric oxygen content with small deviation δ could be expected.

The thickness and roughness parameters of each layer within the two heterostructures, LSMO-final and LSFO-final, were evaluated from the simulation of XRR curve (not shown here) using the Paratt algorithm implemented in GenX [37]. The errors are calculated as 5% increase in the optimal figure of merit (FOM) which is an average of the absolute difference between the logarithms (base 10) of the data and simulation. The obtained values are listed in table 1. It is observed that roughness of the interface layers is in the order of one atomic unit cell (∼4 Å or 1 monolayer) indicating a sharp interface. The reduced surface layer thickness, e.g. LSFO (LSMO) layer in LSFO-final (LSMO-final) can be attributed to aging effects, such as, loss of oxygen at the surface resulting in a reduced density, whereas the interface between both layers is not affected. As mentioned earlier, the thickness obtained from the XRD oscillations represents thicknesses of the crystalline part of the sample, while XRR reveals the thickness information of the entire structure irrespective of ordered or disordered (e.g. amorphous) layers. From the comparison, it can be concluded that the excess thickness obtained from the XRR comes from the contribution of amorphous/non-crystalline surface layer, formed due to aging effect at the surface [38].

Figure 4 shows the high-resolution HAADF STEM images of the interfaces between the deposited layers of LSMO-final (left) and LSFO-final (right), where the white dashed line

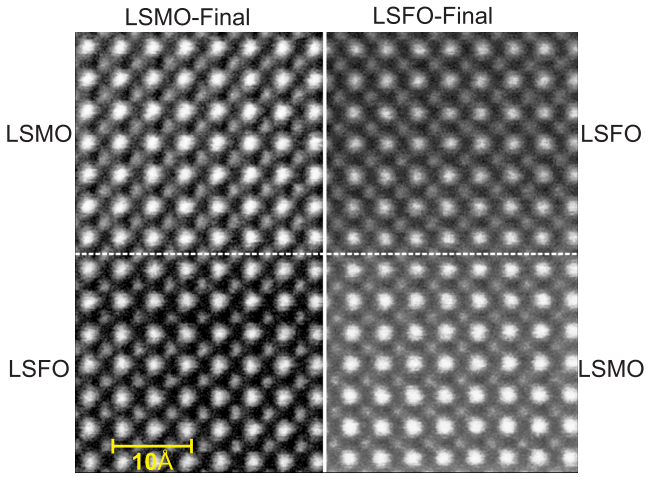

Figure 4. STEM-HAADF measurement for LSMO-final (left) and LSFO-final (right), respectively. The dotted white line estimates the interface between LSFO and LSMO.

describes the interface between LSMO and LSFO layer. From the measurement it is possible to identify the La/Sr (A-site) columns by larger and Fe/Mn (B-site) columns by smaller HAADF intensity peaks, forming the pseudo-cubic perovskite structure with an average lattice constant of 3.86 Å in both directions, i.e. $a = c$. This holds true for both structures and agrees well to the out-of-plane lattice constant c obtained from the XRD measurement.

From the TEM overview scan a lateral correlation of more than 650 Å can be assumed as no defects were visible. This is also in accordance to the LEED measurement of the surface (not shown here), which revealed a high degree of lateral ordering observed by scanning of the electron beam over the surface. The electron coherence radius in the LEED measurement can be estimated to be larger than 100 Å and thus is in agreement with the TEM measurement. The STEM measurements are in good agreement with the XRD and LEED results, which indicates epitaxy both in lateral and growth direction, respectively. Therefore, an epitaxial growth of LSMO/LSFO/STO(0 0 1) and LSFO/LSMO/STO(0 0 1) without evident crystal failures or distortions can be deduced.

Figures 5(a) and (c) shows the element specific mapping of Mn and Fe measured for LSMO-final and LSFO-final, respectively, performed with EDX spectroscopy. An integration of the intensity in rows parallel to the surface is shown in figures 5(b) and (d), respectively and from the comparing it can be immediately observed that—(i) for the LSMO-final, while the Mn signal decays exponentially within LSFO region, distinct oscillations of the Fe signal (∼7 monolayers) could be observed inside the nominal region of LSMO, indicating interdiffusion of Fe, and (ii) for LSFO-final, both the Fe and Mn signal decays exponentially on either side of the interface indicating no intermixing at the interfaces. Delocalization of the EDX signal over distances of more than a unit cell is expected due to multiple and thermal diffuse scattering of the electron probe in a 20 nm to 50 nm thick sample [39].

The negligible interdiffusion in LSFO-final is in clear contrast to the much stronger diffusion of Fe in the LSMO

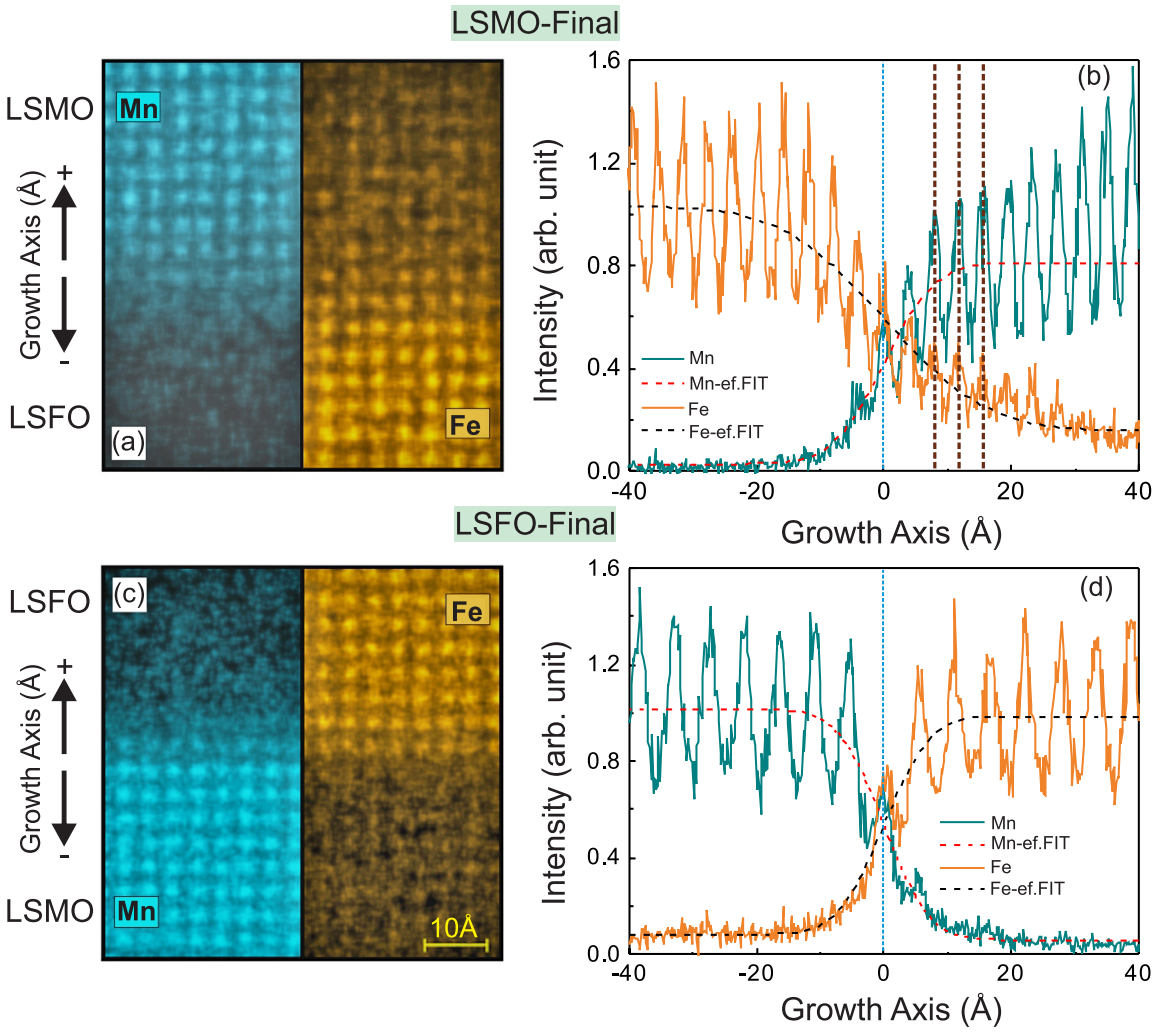

Figure 5. (a) Elemental mapping and (b) laterally integrated EDX signal, of the Mn and Fe content for the LSMO-Final. (c) and (d) Shows the same for sample LSFO-final. The growth axis denotes the growth direction with the value zero and negative (positive) corresponding to the interface and layer close to the substrate (surface), respectively. The brown dotted lines in (b) indicate the B-site atoms, which are equal for Mn and diffused Fe. The profile indicated with dotted lines in both (b) and (d) were obtained by fitting error function to the intensity profile of Fe and Mn; see text section 4. The blue dashed line at the growth axis = 0 Å estimates the interface between LSMO and LSFO.

layer of LSMO-final, where the signal persists within at least seven monolayers distance from the interface. Hence, we state that LSMO-final exhibits strong interdiffusion of Fe into the LSMO layer, but no significant interdiffusion of Mn into the LSFO layer (see discussion in section 4). A careful look at figure 5(b) (for LSMO-final) also reveals that the average oscillation amplitude within the LSMO layer decreases for Mn and consequently increases for Fe while moving toward the interface. This indicates that Fe diffuses near the interface into the LSMO and replaces the Mn atoms at the B-site leading to the formation of a compound $La_{2/3}Sr_{1/3}Mn_{1-x}Fe_xO_3$ inside the LSMO layer. Indicated by brown dotted lines in the figure one can also see that the diffused Fe atoms occupy the Mn positions in LSMO. Moving away from the interface the diffused Fe content decreases within the LSMO layer and stoichiometric condition of the LSMO persists.

3.2. Depth-resolved magnetization

Macroscopic magnetization measurements (using SQUID) reveal different magnetic properties for the two structures. Figures 6(a) and (b) show the magnetization ($M - H$) measurement of the LSMO-final and LSFO-final, respectively, after field-cooling to 10 K in 3 mT. It is observed that the LSMO-final exhibits no exchange bias effect and has hysteresis behavior similar to a single LSMO layer. This indicates that the interface coupling is either very weak or destroyed because of strong interdiffusion of Fe into the LSMO layer. However, LSFO-final with its sharp interface, shows a clear shift by $\mu_0 H_E = -2.35$ mT (see inset figure 6(b), bottom-right) that relates to the exchange bias effect due to a FM/AF interface coupling [40]. Such exchange bias effect, if present, could not be detected at higher temperatures as the observed coercive field <0.1 mT (see inset figure 6(b), top-left) was

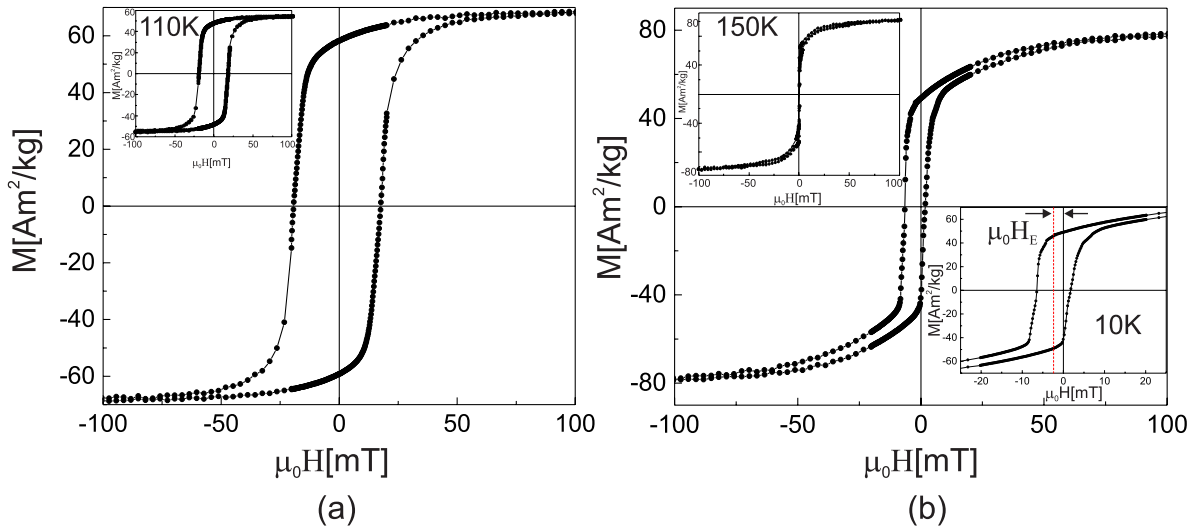

Figure 6. Magnetic hysteresis at 10K, measured after 3 mT field-cooling, for (a) LSMO-final where the inset show measurement at 110 K and (b) LSFO-final heterostructure, where the inset on bottom-right show the zoomed in plot revealing the clear shift (marked with red dashed line) indicating the exchange field $\mu_0 H_E = -2.35$ mT, and on top-left corner the magnetization measurement at 150 K after field cooling at 1 T is shown.

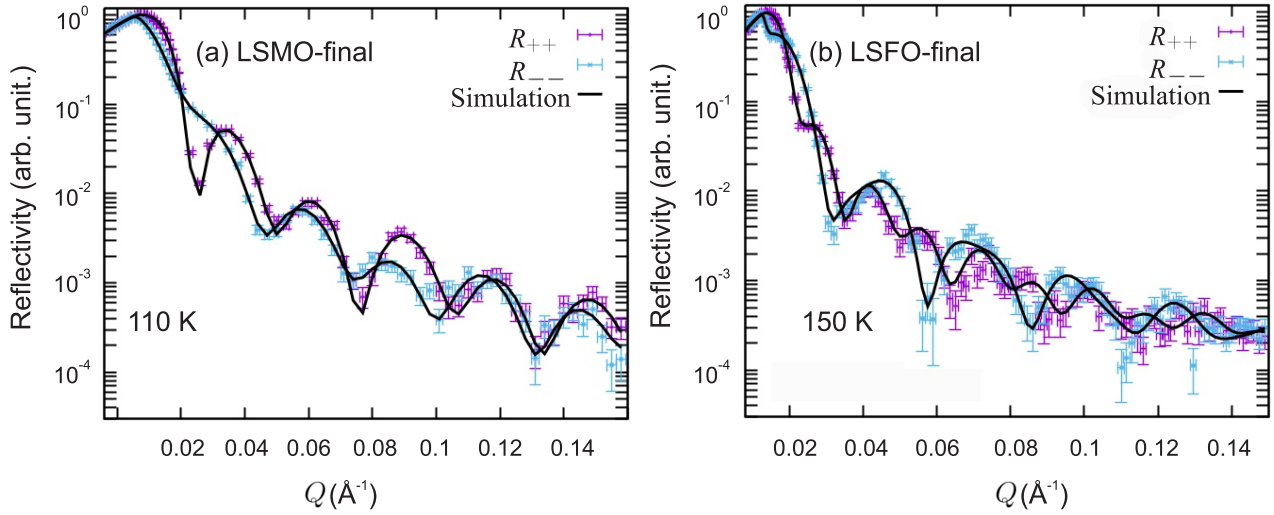

Figure 7. (a) PNR measurement of sample LSMO-final at 110 K including the simulation, and (b) shows a measurement performed on LSFO-final at 150 K.

fairly small and at the resolution limit of the measuring instrument.

In order to understand the underlying interaction mechanism, we resolve the magnetization depth profile of the two structures along the growth direction (z-axis) for different temperatures, using PNR. The interdiffusion has a large influence on the subtle balance of the ions and strain at the interface and as a consequence it affects the magnetic properties significantly. PNR unravels the difference in magnetic depth profile caused by the change in sensitive balance of ions at the interface. At the saturation field of the ferromagnetic LSMO layer the intensity of the spin-flip reflectivities reaches almost zero for both the heterostructures. Therefore, in the following we discuss only measurement of the non-spin flip channels, which gives information about the structure and magnetization component parallel to the applied magnetic field.

Figure 7 depicts PNR measurements and simulations for LSMO-final and LSFO-final, at 110 K and 150 K, respectively. The specific temperatures are chosen so that the magnetization of the LSMO layer is saturated and the LSFO layer is in an AF ordered state. A magnetic field of 110 mT is applied to saturate the magnetization of the LSMO layer parallel to the neutron polarization (i.e. $\vec{M} \parallel \vec{P}$). Both the measured reflectivities (R_{++} and R_{--}) show clear oscillations, however with distinctively different features. To quantify the differences between both samples the PNR curves have been analyzed by simulating the data in GenX [37], which uses an adaptive layer segmentation model where one can define the structure of the nuclear and magnetic SLD separately. We emphasize here that, unlike the low x-ray contrast, neutrons show large contrast variation between the LSMO and LSFO layer as Mn features a negative scattering length of -3.75 fm compared

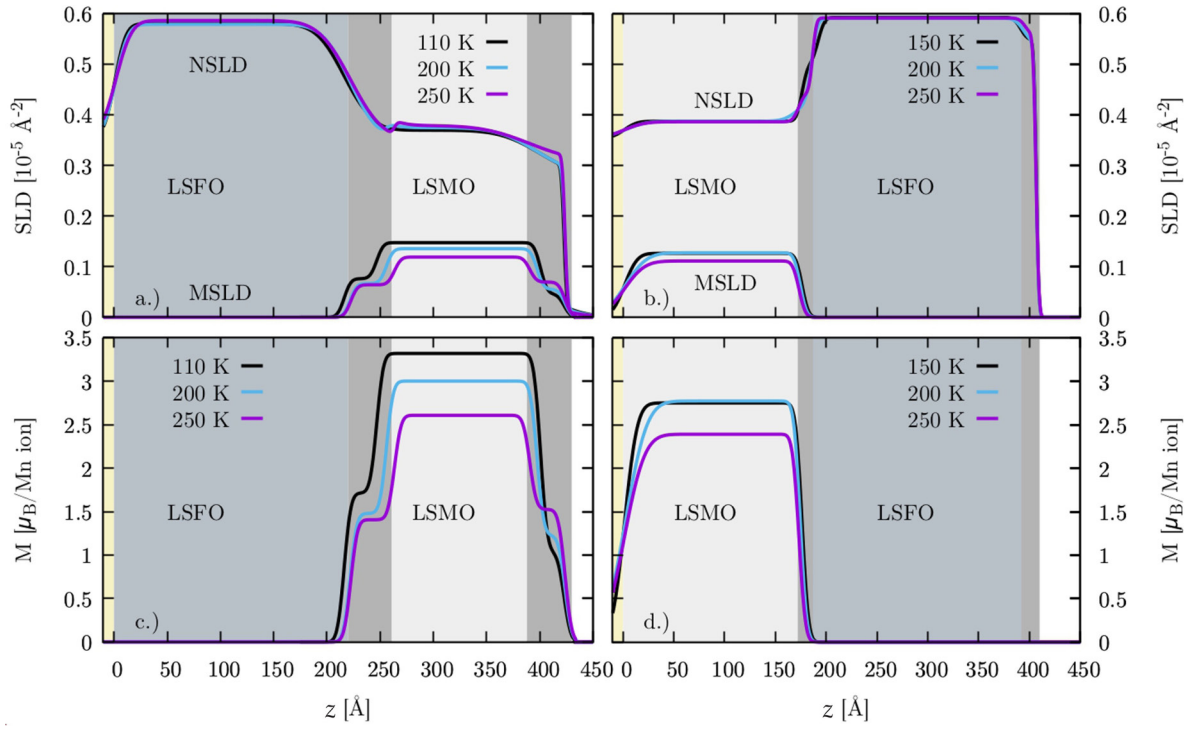

Figure 8. Nuclear (N) and magnetic (M) scattering length density (SLD) obtained from the simulations for (a) LSMO-final, and (b) LSFO-Final. The magnetization development in μ_B/Mn ion is shown for the same samples in (c) and (d), respectively. The origin of the z scale is defined as the STO(0 0 1) substrate surface.

to 9.45 fm for Fe. For simulation of the magnetic profile, the adopted model was kept simple considering only one additional magnetic layer at the interface and a reduced/magnetic-dead-layer on the surface [38, 41] of the heterostructure. It is observed that this model fits well and keeps the amount of fitting parameters reasonably low [29].

Similar reflectivity curves were obtained from the measurements done at different temperatures and were used for further simulations. Figures 8(a) and (b) show the nuclear(N)-SLD together with the magnetic(M)-SLD of both samples for different temperatures. A closer look on the NSLD reveal that the interface is smeared for the sample LSMO-final and shows a higher surface roughness. This extended interface width is in good agreement with the EDX measurements discussed before. In contrast, the sample LSFO-final exhibits a sharp and well defined interface, which is also in accordance to the EDX results. The simulation also reveal a surface layer with reduced NSLD of thickness ∼34 Å and 17 Å respectively for LSMO-final and LSFO-final. This is in good agreement to the thickness obtained from the XRR measurements (table 1), however higher values of the surface layer thickness could be attributed to various aspects such as, aging effects, adsorption/loss of surface oxygen, different measuring environment and technique (x-rays and neutrons) used.

Figures 8(c) and (d) show the magnetization depth profile in μ_B/Mn atom also obtained from the simulations. Temperatures greater than 100 K were chosen to avoid an additional strain effect due to the antiferrodistortive phase transition in STO which adversely influences the magnetization in LSMO [42]. In order to study the coupling effect between the electronic states within the LSFO layer and the magnetization of the LSMO layer the measurements are done at temperatures above (250 K), near (200 K) and below (110 K and 150 K) the Verwey transition of LSFO. However, in both the structures (LSMO and LSFO-final), no appreciable change in the magnetization of the interface or LSMO layer is observed as the system is moved through the Verwey transition of the LSFO. Interestingly this reveals that, at the interface, no or negligible coupling exists between the electronic states of the AF-layer and magnetization of the FM-layer in such heterostructures, irrespective of the growth order. One possible reason could be because the coupling effect is very small and easily destroyed at the interface due to strain or roughness. The small difference in height of the magnetization in the LSMO layer, for the two heterostructures, might be attributed to a non-sufficient field to saturate the sample (as seen from inset figure 6(b)) or to strain effects.

For both samples, the fit model ensures a reduced magnetization in the surface region. Such a magnetic dead layer has also been observed before [38, 41]. It has been attributed to oxygen deficiencies, which weaken either the double exchange or superexchange and hence any magnetic order and the electronic properties. Oxygen vacancies at interfaces appear during the growth process caused by high temperatures and low oxygen partial pressure. Usually, post-growth annealing avoids oxygen deficiencies, but for thicker films they can persist.

Nevertheless, a striking difference in the magnetization profile at the interface can be observed for the two heterostructures. For LSMO-final (figure 8(c)) best fit was obtained for a structure with an extended interface region where the magnetization drops to about 50% (∼1.5 μ_B/Mn atom) of the

magnetization value in the middle of the LSMO layer (∼3.0 μ_B/Mn atom). The interface is observed to be extended on the LSMO side of the interface and has a thickness of 31 ± 3 Å. This is in good agreement with the EDX results which show interdiffusion within seven monolayers. As the Fe moments are always oriented perpendicular to the Mn moments [43], the reduced magnetization in the interface can be directly linked to the diffusion of Fe into Mn-sites (as seen from EDX). Chérif *et al* [44] observed that the magnetization in such systems is destabilized due to the different ion size of Fe which occupies a B-site formerly occupied by a Mn ion, which also leads to a change in the applied strain within the interface region. The destabilization leads to a reduced saturation magnetization and decrease of T_C.

The LSFO-final shows a homogeneous magnetization in the entire LSMO layer. The transition regions between substrate and LSMO, and between LSMO and LSFO extend over a similar range as determined by the XRR and EDX. The interface appears sharp and the magnetization decays rapidly to zero towards LSFO with no significant net magnetization in the AF region. The sharp magnetization profile correlates with the EDX results, which shows only small or no interdiffusion. Thus, with no reduced magnetization profile at the interface, one could expect a strong FM/AF exchange bias coupling between the LSMO and LSFO layer, as evident from the $M - H$ measurements.

4. Discussion

In this study we have observed that high quality epitaxial heterostructures of LSFO and LSMO can be grown combining different growth methods and that the in-air transport between the growth chambers is not detrimental to the film quality. However, the interface between both layers varies drastically depending on the growth order. The growth of LSMO by sputtering on LSFO/STO(0 0 1)—shows strong diffusion of Fe into the LSMO close to the interface, resulting in a Fe-doped region of $La_{2/3}Sr_{1/3}Mn_{3-x}Fe_xO_3$ with reduced magnetization. While in the MBE grown LSFO on sputtered LSMO/STO(0 0 1) sharp interface with no or small diffusion is detected.

To get a deeper insight into the interdiffusion process, we analyzed our EDX results of figures 5(b) and (d) using Fick's second law [45] for non-steady state diffusion across an interface as a function of time and position. As the intensity obtained from the EDX measurement is directly proportional to the respective atomic concentration in the layers, the profile can be fitted to an error function (*erf*) as [46],

$$\frac{c(z,t) - c_1}{c_2 - c_1} = \frac{1}{2}\{1 + erf[D^*(z - z_0)]\} \qquad (1)$$

where c_1 is the concentration of a diffusing species in its source compound (e.g. Fe in LSFO), c_2 is the minimum concentration in the target compound (e.g. Fe in LSMO). $c(z,t)$ is the concentration of a component at a position z perpendicular to the interface at time t. In the present case, t denotes the time at which equilibrium concentration is reached on both sides of the interface under the sample preparation environment. z_0 is estimated as the position where concentration of the element decreases to $(c_1 - c_2)/2$. The effective reciprocal diffusion constant (D^*) is defined as,

$$D^* = \frac{1}{\sqrt{4Dt}} \qquad (2)$$

with D being the respective diffusion constant. The values of D^* obtained from the fit are listed in table 2 and the error functions are plotted as dotted lines in figures 5(b) and (d), respectively for the two structures. The numerical error of fit is estimated from one standard deviation of the fitting parameter.

Table 2. Effective reciprocal diffusion constant D^* (in $Å^{-1}$) obtained by fitting the Fe and Mn EDX profile in figures 5(b) and (d) to equation (1).

	Fe	Mn
LSMO-final	0.55 ± 0.03	1.11 ± 0.03
LSFO-final	1.24 ± 0.05	1.26 ± 0.05

From the fittings it could be observed that D^* is same for both Fe and Mn in LSFO-final. This means that at the interface, concentration of both elements drops with the same rate, i.e. indicating no interdiffusion. However, for LSMO-final two observations can be made: (i) the value of D^* for Mn is smaller than in LSFO-final indicating increased diffusion of Mn at the interface, and (ii) the value of $D^*_{Fe} < D^*_{Mn}$ revealing ∼50% more diffusion of Fe than Mn at the interface. This is astonishing as the growth rates/ fluxes viz. the thermal energy of atoms for both growth methods were nearly identical and therefore the order of deposition method should not have an impact. Also the bulk diffusion constants (D) for both Fe and Mn should not change with the deposition order as the growth temperature were same for both the heterostructures. Therefore, the difference must rather be directly related to the growth process itself.

In the case of LSMO-final, where the LSMO layer is sputtered onto the pre-grown LSFO layer, the small target-to-sample distance within the sputtering chamber leads to an increased kinetic energy and backsputtering. This results in the redeposition [47] of surface-near atoms caused by the oxygen plasma located close to the sample surface. The effect is presumably stronger for Fe due to its lower mass compared to La and Sr, therefore allowing Fe ions from near-surface layers to easily move over the surface. Now, at high growth temperature (1250 K), essential for epitaxial growth, the Mn partial pressure is about seven orders of magnitude higher than that of Fe [48]. Also the high pressure in the sputtering process thermalizes the sputtered target material. This leads to a high desorption of Mn in the high oxygen pressure environment while it is sputtered from the solid LSMO target during growth. This is also true when one considers different volatile manganese oxides (Mn_2O_3, MnO_2) forming under such conditions. The loss of Mn, therefore creates B site vacancies in the perovskite structure which can then be occupied by the free Fe ions at the surface. As the growth continues, due to limited free Fe-ions at the LSFO surface and with increasing thickness of

the LSMO top layer, stoichiometric condition prevails in the LSMO. Sr and La are not affected by this mechanism as SrO and La_2O_3 are very stable at high temperatures due to their high melting points of 2800 K and 2588 K, respectively.

While in case of LSFO-final, the LSMO layer is first grown on to the STO(0 0 1) substrate in the sputtering chamber. Therefore, even though desorption of Mn takes place at the growth condition there are no free ions that could replace the Mn-sites and stoichiometric condition prevails with the increasing thickness of the LSMO layer. After the growth, the sample is cooled down to room temperature under the high oxygen pressure which leads to the saturation of the sample w.r.t. oxygen and therefore is stable even at higher temperatures. Now, when it is transferred to the MBE chamber for the growth of the LSFO layer, due to large cell-to-sample distances and low oxygen partial pressure, the kinetic energy of the surface-near atoms would not be sufficient enough to overcome the surface-free energy. Additionally, the oxides, most likely Fe_2O_3 during growth in a low pressure oxygen atmosphere, is very stable at high temperature and a desorption is unlikely. Thus leading to atomically sharp LSFO/LSMO interface with very low or almost vanishing intermixing.

5. Summary

We have investigated the structural and magnetic properties of LSFO/LSMO heterostructures, which were successfully grown epitaxially on STO(0 0 1) substrate with a combination of two established growth methods—the MBE and HOPS. Significant differences can be found in two samples which exhibit a different growth order and can be related to the kinetics involved in the two growing methods. The system LSMO-final shows a significant interdiffusion of Fe in at least 7 monolayers of the LSMO layer near the interface. Depositing LSMO on LSFO leads to occupation of Fe ions at the Mn sites in this region of the LSMO layer. The intermixed region at the interface shows a suppressed magnetization and as consequence does not exhibit an exchange bias effect due to lack of exchange coupling between the FM/AF layer. The thickness ($\sim$31 Å) of this region obtained with PNR is in good agreement with the EDX results. Such a behavior cannot be observed in the LSFO-final heterostructure where a sharp interface with regard to interdiffusion and magnetization is present. The proximity of a ferromagnetic and an antiferromagnetic layer leads to the observed exchange bias effect. Thus, by combination of an element (e.g. EDX) and a magnetization (e.g. PNR) specific interface characterization we can relate details of the growth process to the magnetic properties and hence the functionality of the interface. Therefore, making a valuable contribution in understanding the magnetic properties at a technologically promising FM/AF interface in all oxide perovskite heterostructure.

Acknowledgments

We acknowledge the support of National Institute of Standards and Technology (NIST), US Department of Commerce, in providing the neutron research facilities used in this work.

ORCID iDs

A Sarkar https://orcid.org/0000-0002-2744-0378

References

[1] Dagotto E 2005 *Science* **309** 257–62
[2] Granozio F M, Koster G and Rijnders G 2013 *MRS Bull.* **38** 1017–23
[3] Liu Y, Lucy J M, Glavic A, Ambaye H, Lauter V, Yang F Y and te Velthuis S G 2014 *Phys. Rev.* B **90** 104416
[4] Yamada H, Ogawa Y, Ishii Y, Sato H, Kawasaki M, Akoh H and Tokura Y 2004 *Science* **305** 646–8
[5] Huijben M, Liu Y, Boschker H, Lauter V, Egoavil R, Verbeeck J, te Velthuis S G E, Rijnders G and Koster G 2015 *Adv. Mater. Interfaces* **2** 1400416
[6] He C *et al* 2012 *Phys. Rev. Lett.* **109** 197202
[7] Ke X, Belenky L J, Lauter V, Ambaye H, Bark C W, Eom C B and Rzchowski M S 2013 *Phys. Rev. Lett.* **110** 237201
[8] Liu Y, Cuellar F A, Sefrioui Z, Freeland J W, Fitzsimmons M R, Leon C, Santamaria J and te Velthuis S G E 2013 *Phys. Rev. Lett.* **111** 247203
[9] Bruno F Y *et al* 2015 *Nat. Commun.* **6** 6306
[10] Hemberger J, Krimmel A, Kurz T, Krug von Nidda H A, Ivanov V Y, Mukhin A A, Balbashov A M and Loidl A 2002 *Phys. Rev.* B **66** 094410
[11] Guo H *et al* 2016 *Adv. Mater. Interfaces* **3** 1500753
[12] Li J, Sun L, Shenai P M, Wang J, Zheng H and Zhao Y 2015 *J. Alloys Compd.* **649** 973–80
[13] Picozzi S, Ma C, Yang Z, Bertacco R, Cantoni M, Cattoni A, Petti D, Brivio S and Ciccacci F 2007 *Phys. Rev.* B **75** 094418
[14] Adamo C *et al* 2009 *Appl. Phys. Lett.* **95** 112504
[15] Schumacher D, Steffen A, Voigt J, Schubert J, Brückel T, Ambaye H and Lauter V 2013 *Phys. Rev.* B **88** 144427
[16] Li H F, Su Y, Persson J, Meuffels P, Walter J M, Skowronek R and Brückel T 2006 *J. Phys.: Condens. Matter* **19** 016003
[17] Li H F, Su Y, Persson J, Meuffels P, Walter J M, Skowronek R and Brückel T 2007 *J. Phys.: Condens. Matter* **19** 176226
[18] Cao J, Tao S X, Bobbert P A, Wong C P and Zhao N 2018 *Adv. Mater.* **30** 1707350
[19] Vila-Fungueiriño J M, Bui C T, Rivas-Murias B, Winkler E, Milano J, Santiso J and Rivadulla F 2016 *J. Phys. D: Appl. Phys.* **49** 315001
[20] Wang K, Tang M H, Xiong Y, Li G, Xiao Y G, Zhang W L, Wang Z P, Li Z and He J 2017 *RSC Adv.* **7** 31327–32
[21] Sichel-Tissot R J, Devlin R C, Ryan P J, Kim J W and May S J 2013 *Appl. Phys. Lett.* **103** 212905
[22] Shimony U and Knudsen J M 1966 *Phys. Rev.* **144** 361–6
[23] Verwey E J W 1939 *Nature* **144** 327–8
[24] Battle P D, Gibb T C and Lightfoot P 1990 *J. Solid State Chem.* **84** 271–9
[25] Devlin R C, Krick A L, Sichel-Tissot R J, Xie Y J and May S J 2014 *J. Appl. Phys.* **115** 233704

[26] Xie Y J, Scafetta M D, Moon E J, Krick A L, Sichel-Tissot R J and May S J 2014 *Appl. Phys. Lett.* **105** 062110
[27] Minohara M, Kitamura M, Wadati H, Nakao H, Kumai R, Murakami Y and Kumigashira H 2016 *J. Appl. Phys.* **120** 025303
[28] Urushibara A, Moritomo Y, Arima T, Asamitsu A, Kido G and Tokura Y 1995 *Phys. Rev.* B **51** 14103–9
[29] Waschk M 2017 Interface phenomena in $La_{1/3}Sr_{2/3}FeO_3$/$La_{2/3}Sr_{1/3}MnO_3$ heterostructures and a quest for p-electron magnetism *PhD Thesis* RWTH Aachen University
[30] Monsen Å, Boschker J E, Macià F, Wells J W, Nordblad P, Kent A D, Mathieu R, Tybell T and Wahlström E 2014 *J. Magn. Magn. Mater.* **369** 197–204
[31] Ankner J F and Felcher G P 1999 *J. Magn. Magn. Mater.* **200** 741–54
[32] 2017 *Polarized Beam Reflectometer (PBR)* NIST Centre for Neutron Research (https://www.ncnr.nist.gov/instruments/pbr)
[33] Kruth M, Meertens D and Tillmann K 2016 *J. Large-Scale Res. Facil.* **2** A59
[34] Schlossmacher P, Klenov D, Freitag B, von Harrach S and Steinbach A 2010 *Microsc. Anal.* **24** S5–8
[35] Blasco J, Snchez M, Garca J, Stankiewicz J and Herrero-Martn J 2008 *J. Cryst. Growth* **310** 3247–50
[36] Dhahri N, Dhahri A, Dhahri J, kebir Hlil E and Dhahri E 2013 *J. Magn. Magn. Mater.* **326** 129–37
[37] Björck M and Andersson G 2007 *J. Appl. Crystallogr.* **40** 1174–8
[38] Borges R P, Guichard W, Lunney J G, Coey J M D and Ott F 2001 *J. Appl. Phys.* **89** 3868–73
[39] Spurgeon S R, Du Y and Chambers S A 2017 *Microsc. Microanal.* **23** 513–7
[40] Rana R, Pandey P, Singh R P and Rana D S 2015 *Sci. Rep.* **4** 4138
[41] Zakalek P 2016 Magnetic interface effects in thin film heterostructures *PhD Thesis* RWTH Aachen, Forschungszentrum Jülich GmbH
[42] Mota D A *et al* 2014 *J. Phys. D: Appl. Phys.* **47** 435002
[43] Arenholz E, van der Laan G, Yang F, Kemik N, Biegalski M D, Christen H M and Takamura Y 2009 *Appl. Phys. Lett.* **94** 072503
[44] Chérif W, Ellouze M, Lehlooh A F, Mahmood S H and Elhalouani F 2012 *Hyperfine Interact.* **211** 153–64
[45] Fick A 1855 *Ann. Phys. Chem.* **170** 59–86
[46] Ashraf T, Sarkar A, Grafeneder W and Koch R 2018 *J. Appl. Phys.* **124** 215301
[47] Widmann D, Mader H, Friedrich H, Heywang W and Müller R 2000 *Technology of Integrated Circuits* (Berlin: Springer) pp 13–93
[48] Alcock C B, Itkin V P and Horrigan M K 1984 *Can. Metall. Q.* **23** 309–13